SUPPLEMENTARY INFORMATION (SI) FOR

Surface warming in global cities is substantially more rapid than in rural background areas

Zihan Liu[1], Wenfeng Zhan[1, 2*], Benjamin Bechtel[3], James Voogt[4], Jiameng Lai[1], Tirthankar Chakraborty[5, 6], Zhi-Hua Wang[7], Manchun Li[1*], Fan Huang[1], and Xuhui Lee[5*]

1. Jiangsu Provincial Key Laboratory of Geographic Information Science and Technology, International Institute for Earth System Science, Nanjing University, Nanjing, Jiangsu 210023, China
2. Jiangsu Center for Collaborative Innovation in Geographical Information Resource Development and Application, Nanjing 210023, China
3. Department of Geography, Ruhr-University Bochum, 44801 Bochum, Germany
4. Department of Geography, Western University, London, Ontario, Canada, N6A 5C2
5. School of Forestry and Environmental Studies, Yale University, New Haven, Connecticut 06511, USA
6. Atmospheric Sciences and Global Change Division, Pacific Northwest National Laboratory, Richland, Washington 99354, USA
7. School of Sustainable Engineering and the Built Environment, Arizona State University, Tempe, AZ 85287, USA

*** Corresponding author:** W. Zhan (zhanwenfeng@nju.edu.cn), M. Li (limanchun@nju.edu.cn), and X. Lee (Xuhui.lee@yale.edu).

THIS FILE INCLUDES:

A. Supplementary Notes

Supplementary Notes 1 to 4

B. Supplementary Figures

Supplementary Figures 1 to 16

C. Supplementary Tables

Supplementary Tables 1 to 5

D. Supplementary References

Supplementary References 1 to 31

A. Supplementary Notes

<u>Note 1</u>: *Discussions on different representations between land surface temperature (LST) and surface air temperature (SAT) and on attribution of surface warming*

Satellite-derived LST as well as elaborately characterized transitions in land cover types facilitate the investigation of surface warming of global cities. We are, however, aware of the different representations between LST and SAT in terms of climate change[1] considering that they possess different physical meaning and responses to climate change. LST characterizes a two-dimensional representation of a three-dimensional urban surface[2] – they represent a combination of surface temperature signals from building roofs, walls, urban lawns and tree canopies, and streets[3]. SAT accounts for the warming or cooling of an atmospheric layer or volume from the surface to approximately the mean roof level (i.e., building height)[4]. Furthermore, satellites can only obtain valid LST data under clear skies, while all-weather SAT can be obtainable from reanalysis data. Satellite LSTs are not flawless for measuring surface climate change or, more especially, heat stress. Nevertheless, here we primarily concentrate on warming trend rather than the absolute value, which can reduce the LST-SAT difference significantly. The anomalies between satellite LST and reanalysis SAT over urban core (refer to Supplementary Fig. 3) confirm, to some degree, the potential validity for comparing the trends between these two parameters. We should make clear that the LST-based warming results do not serve as a surrogate for SAT-based analysis, but they provide a different approach that overcomes some limitations or difficulties in finding appropriate urban – rural station pairs of SAT over global cities.

To isolate the contributions from controls to surface warming across global cities consistently, we employed a statistical attribution method that disregards the interactions among controls and that uses population for the proxy of urbanization effect. Part of the reason lies in the difficulty in obtaining times series urban parameters in urban morphology and fabrics across 2000+ cities worldwide. We acknowledge this can over-simplify the complexity in urbanization on surface warming for cities at different development stages. Future work can incorporate detailed urban parameters in surface morphology and surface fabrics towards a more accurate quantification of urbanization effect. In addition, SAT and associated atmospheric urban heat island refers to a warming or cooling of the urban air and directly impacts human health and well-beings[5, 6]. LST provides a direct characterize of surface thermal conditions and plays an important role in regulating SAT through the surface-air exchange[4]. Future attention should be paid to the combination of these two types of temperature, which can improve the interpretation of urban thermal environments and assist in developing effective heat mitigation strategies.

Note 2: *Relationships between LST and population density (or EVI) trends*

We investigated the relationships between LST and population density (or EVI) trends over urban areas across different continents. The rations between LST and population density (or EVI) trends suggest that the global mean LST trend would increase by 0.096 K·decade^{-1} when population density increases by 100/km^2 per decade, while it would decrease by 0.26 K·decade^{-1} when EVI increases by 0.01 per decade (Supplementary Table S4). The ratios between LST and population density (or EVI) trends show variations among continents. The ratios between LST and population density trends in Europe and North America are relatively large, with the mean ratios of 0.21 and 0.29, respectively. While there were relatively small ratios between LST and population density trends in Asia and Africa (with the mean ratios of 0.057 and 0.025 respectively), even though they have more pronounced urban surface warming trend. The reason for such discrepancies might be related to the greater growth rates of population density in Asia and Africa[7]. We further observe that the ratios between LST and EVI trends are smaller in Europe, Africa, and South America than in other regions. This can be attributed to the relatively larger EVI trends in these three regions. For example, the largest regional mean EVI trend occurs in Europe (0.012 ± 0.0032 decade^{-1}), while decreasing trends occur in Africa and South America, with the mean values of −0.0088 ± 0.0031 decade^{-1} and −0.0091 ± 0.0037 decade^{-1}, respectively. The declining EVI trends in Africa and South America may be related to reduction of urban green spaces induced by human activities. These results strongly demonstrate the regional differences in the quantitative relationships between LST and population density (or EVI) trends among continents. They would help provide a rough estimate of future urban surface warming and geographically targeted guidelines for the design of heat mitigation strategies.

Note 3: *Possible uncertainties related to satellite and reanalysis data*

We use satellite land surface temperature (LST) and reanalysis surface air temperature (SAT) data to investigate the contributions of background climate change (BCC), urbanization, and landscape greening on surface warming trends over global cities. The possible uncertainties may occur because of the deficiencies of the used LST and SAT datasets.

We acknowledge that the data error of satellite LST in urban lands may bias the results. Nevertheless, the data processing method and research target in this study would greatly reduce these uncertainties. On the one hand, the surface warming trends across cities were calculated based on all the available surface warming trends at the pixel level. This spatial average process can greatly reduce the possible uncertainties of a certain pixels. On the other hand, the large-scale investigation could substantially suppress the uncertainties in a few cities, according to the 'Central Limit Theorem' (the global deviation would be much smaller than the deviation for a single city especially for a large sample size)[8-10]. More importantly, satellite LST and particularly the MODIS LST product remains indispensable for a global study as such, due to their advantages to provide global coverage, repeatability, consistency, medium spatial resolution (1 km), and free availability of relatively long time series LST observations[11-13].

We used the SAT data as a proxy to investigate the BCC impacts on urban surface warming. The SAT reanalysis data were used to represent the BCC mainly due to the following aspects: (1) BCC can be mainly reflected by SAT and precipitation over the inter- or intra-annual scales[14, 15]. However, here only SAT was included, mainly considering that precipitation has more profound implications for intra-annual and diurnal LST variations rather than inter-annual LST variations[16, 17]. We only used SAT also because the influence of precipitation on LST is difficult to quantify directly by remote sensing, mostly due to the unavailability of satellite LST observations when precipitation event occurs[16, 18]. (2) The SAT reanalysis data were expected to reflect background climate conditions because the current climate models generally do not contain urbanization information signals such as land use and cover changes (Zhao et al., 2021; Zheng et al., 2021). More importantly, previous study has used reanalysis SAT data as a proxy for BCC to investigate the urban warming (or urban heat island) responsive to BCC at the global scale[13, 18].

We acknowledge that reanalysis SAT data may contain urbanization signals induced by data assimilation of different datasets. To suppress the possible uncertainties related to the urbanization signals, we only incorporated the reanalysis SATs over rural areas yet totally discarded the urban ones in this study. We admit that SAT responds both to internal natural variability and external forcing factors[19-22]. Therefore, the identified contribution from BCC to urban surface warming trends may be biased by natural oscillations of SAT in a few cities. Nevertheless, the research topic and target in this study can greatly reduce these uncertainties, mostly due to the following aspects. On the one hand, we mainly focused on the LST-derived surface warming trends rather than SAT-derived atmospheric warming trends. Generally, the LST variations are strongly determined surface biophysical properties, although they are also highly linked to background climate[23-26]. Consequently, the possible uncertainties induced by natural oscillations are expected to be relative weak. On the other hand, despite the unavoidable uncertainties in individual cities, the large-scale investigation could also substantially suppress the uncertainties. This is mainly because the global deviation can be smaller than that of individual cities, according to the Central limit theorem[8, 9].

Nevertheless, we acknowledge that there still exist some residual uncertainties on the identified surface warming trends from natural oscillations of SAT. To better assess the contribution of BCC to the surface warming trends, future endeavors should consider the incorporation of co-trending tests and regression-based decomposition method to separate natural oscillations and external forcing factors[19, 20].

Note 4: *Identification of abrupt changes (breakpoints) in time series LST and enhanced vegetation index (EVI) data*

To classify accurately the urban surfaces and their surroundings into urban core, rural background, and transitional land, the abrupt changes (i.e., breakpoints) in time series LST or EVI data were dectected by the BFAST algorithm. The BFAST algorithm decomposes the time series data into the trend, the seasonal, and the remainder components. The trend component describes an inter-annual change in the time series data, which can contain several segment-specific trends when there exist a single or several breakpoints[27]. The seasonal component describes the periodic variation of LST or EVI data within an annual cycle, primarily driven by the annual variation in incoming solar radiation[27, 28]. The seasonal variations of LST and EVI can be approximated by a widely used sinusoidal function[27, 29]. The noise component is an irregular variation in LST or EVI data induced by atmospheric conditions (e.g., cloud coverage and aerosols), and disturbance events (e.g., flood and fire), etc.[29]. The BFAST algorithm has been shown capable of identifying such abrupt changes[27]. When tested with the LST and EVI data, this algorithm demonstrates a relatively high accuracy (Supplementary Fig. 14). The breakpoints (both the breakpoint number and date) using LST data are often consistent with those using EVI data (Supplementary Fig. 15). This result indicates the close connection between LST and EVI as well as the robustness of this algorithm.

We find that more than 30% of the global cities are detected significantly with LST and EVI breakpoints based on hypothesis-testing. These breakpoints mainly occur from 2006 to 2012 and they are often overlapped with the newly urbanized areas (Supplementary Fig. 15). However, the breakpoints are not completely overlapped with these newly urbanized areas because abrupt thermal changes may occur over intra-urban surfaces (e.g., due to urban redevelopment and urban renewal). The results reveal that 63% of the cities detected with significant breakpoints appear in Asia and Africa, while few occur in Europe (Supplementary Fig. 16). This occurrence is associated with the difference in urbanization (urban expansion) among continents – rapid urbanization has been witnessed in Asia and Africa in recent decades[30], while urbanization has been relatively slow in Europe[31].

B. Supplementary Figures

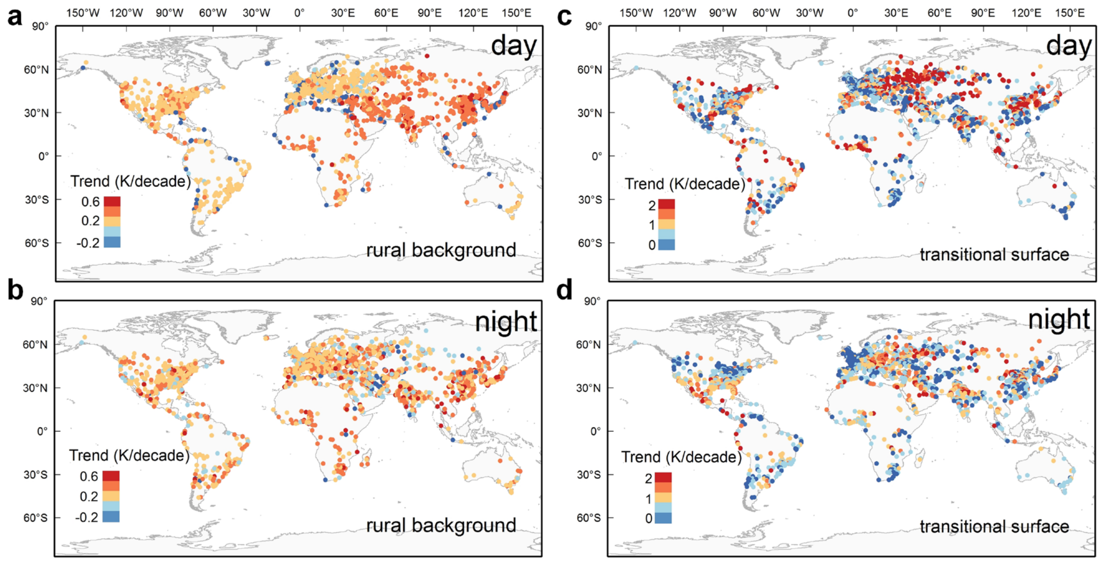

Supplementary Fig. 1 | Warming trends over rural background and transitional surface. Map of daytime trend over rural background (**a**) and transitional surface (**c**), and map of nighttime trend over rural background (**b**) and transitional surface (**d**).

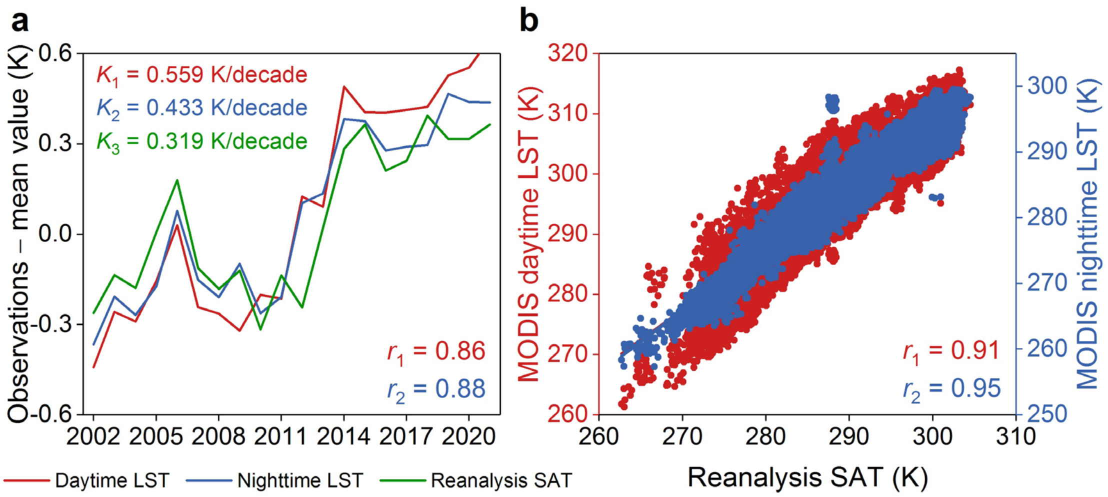

Supplementary Fig. 2 | Comparison between MODIS land surface temperature (LST) and reanalysis surface air temperature (SAT) over urban core. Temporal anomalies (**a**) and statistical relationships (**b**) between MODIS LST and reanalysis

SAT. K_1 to K_3 are the trends (K·decade^{-1}) for daytime LST, nighttime LST, and reanalysis SAT, respectively, and r_1 and r_2 are the Pearson's correlation coefficients between MODIS LST and reanalysis SAT for daytime and nighttime, respectively.

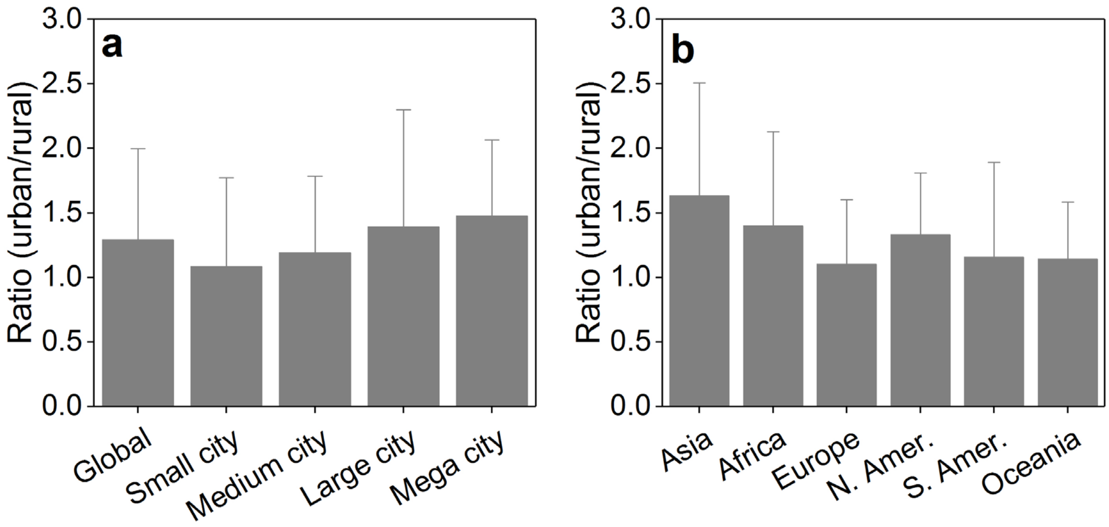

Supplementary Fig. 3 | The ratio of surface warming trend between urban core and rural background by city size and continent. Note that the error bars represent 10% ~ 90% percentiles.

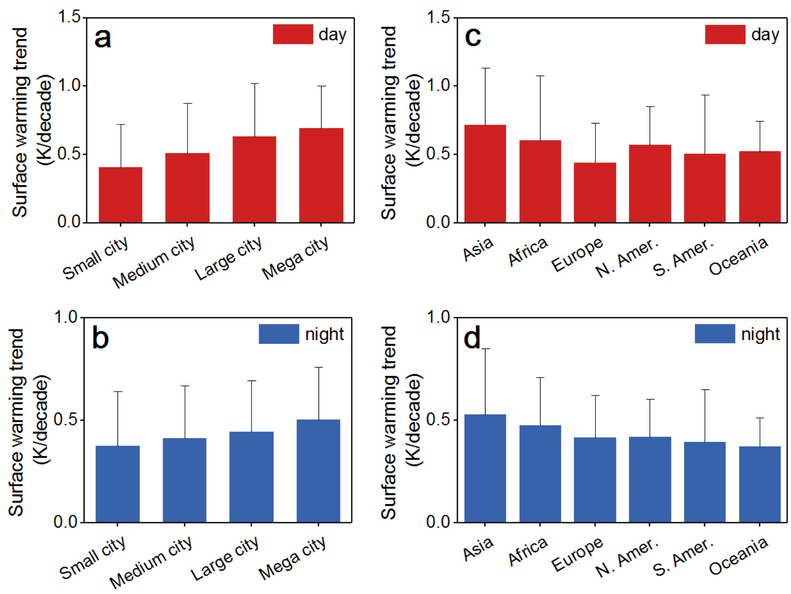

Supplementary Fig. 4 | Surface warming trend at the rural background by city size and continent. Note that the error bars represent 10% ~ 90% percentiles.

222

223

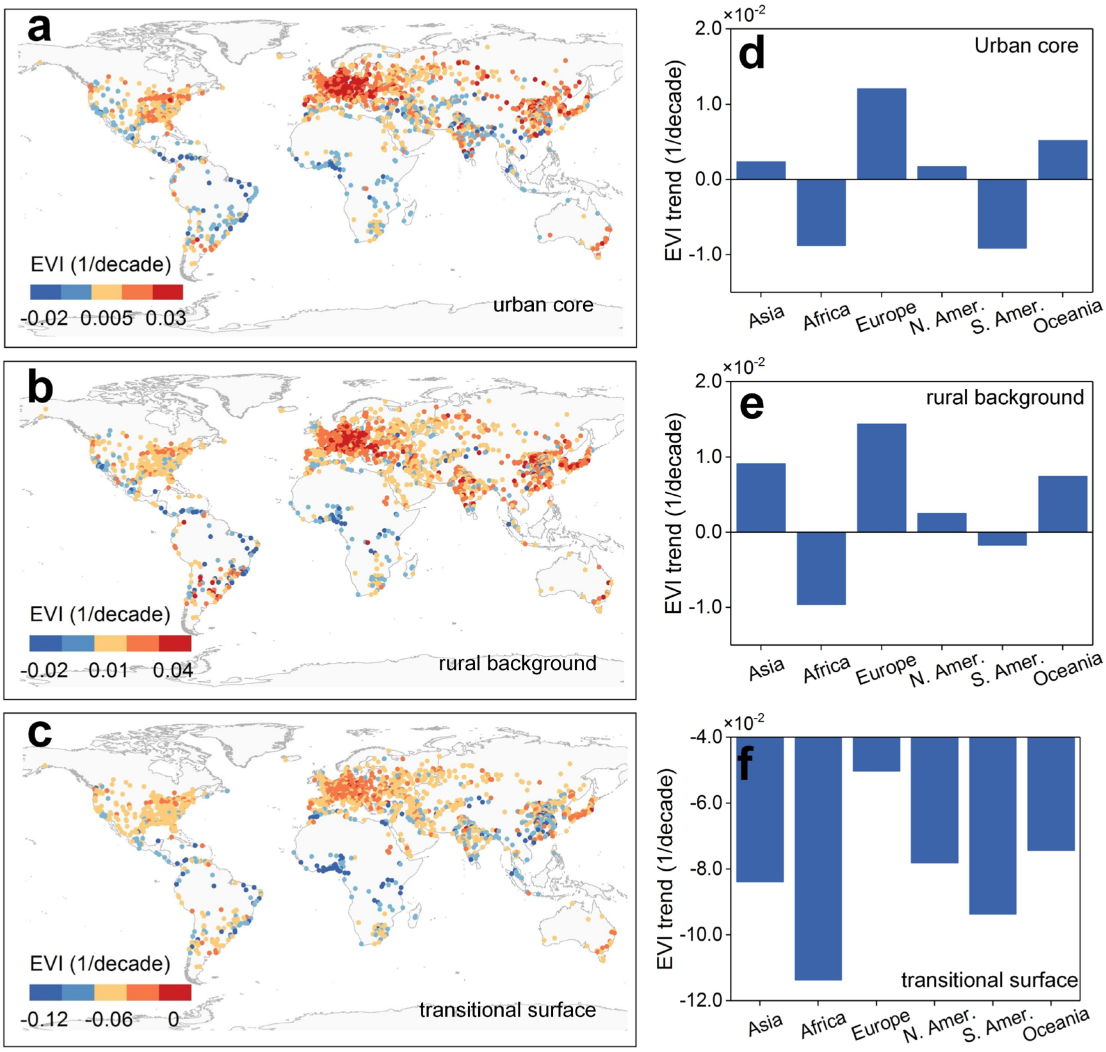

224 **Supplementary Fig. 5 | Urban greening trends (decade^{-1}) characterized by**

225 **enhanced vegetation index (EVI) across the world.** Maps of trends over urban core

226 (**a**), rural background (**b**), and transitional surface (**c**), and continental mean trends

227 over urban core (**d**), rural background (**e**), and transitional surface (**f**).

228

229

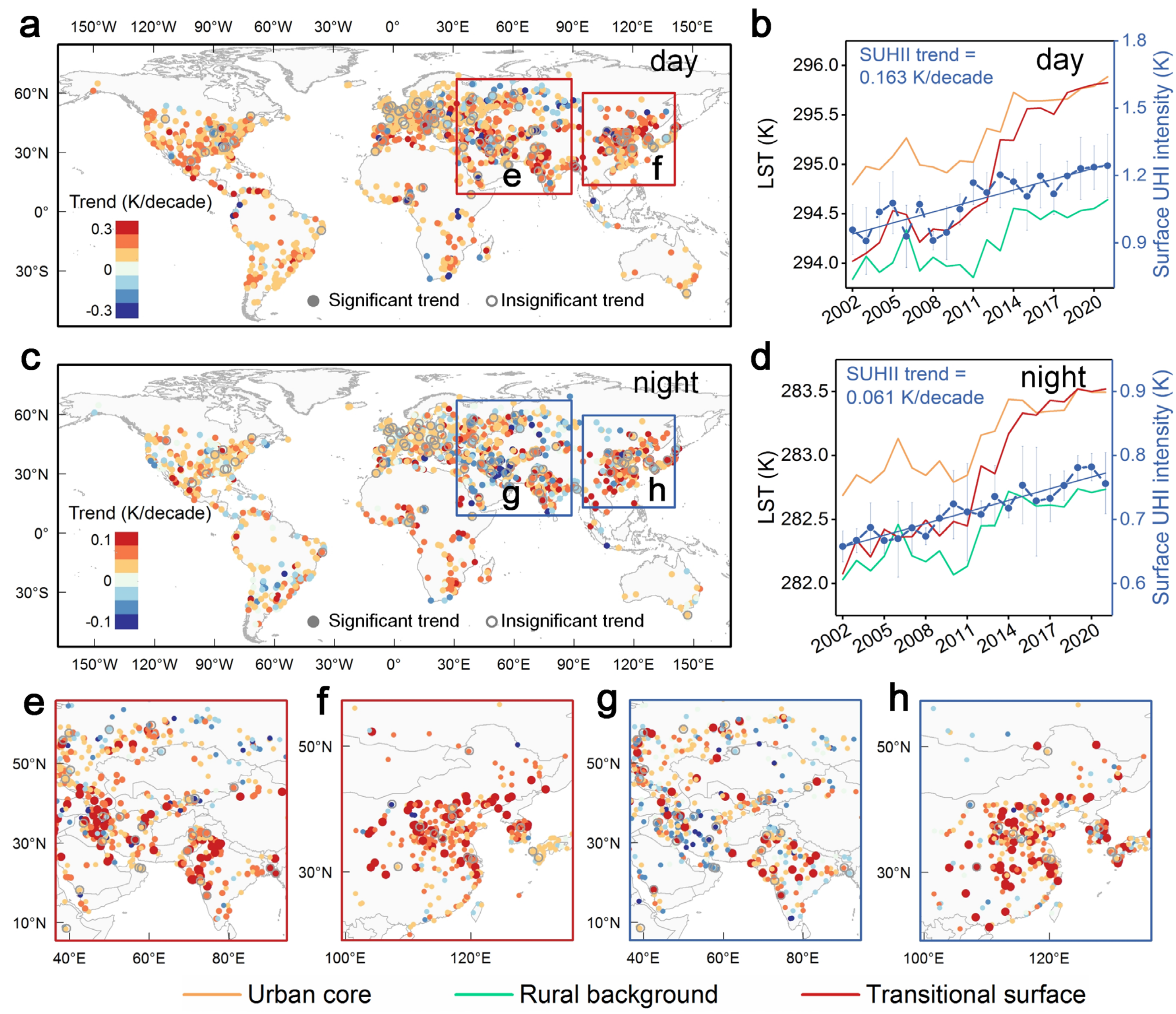

Supplementary Fig. 6 | Surface UHI intensity trends across the world. Map of daytime trend (**a**), map of nighttime trend (**c**), and surface UHI intensity trends in daytime (**b**) and nighttime surface UHI intensity trends (**d**). The two boxed regions in (**a**) and (**c**) are enlarged as (**e**) and (**f**) for daytime and (**g**) and (**h**) for nighttime. Note that the error bars represent 10% ~ 90% percentiles.

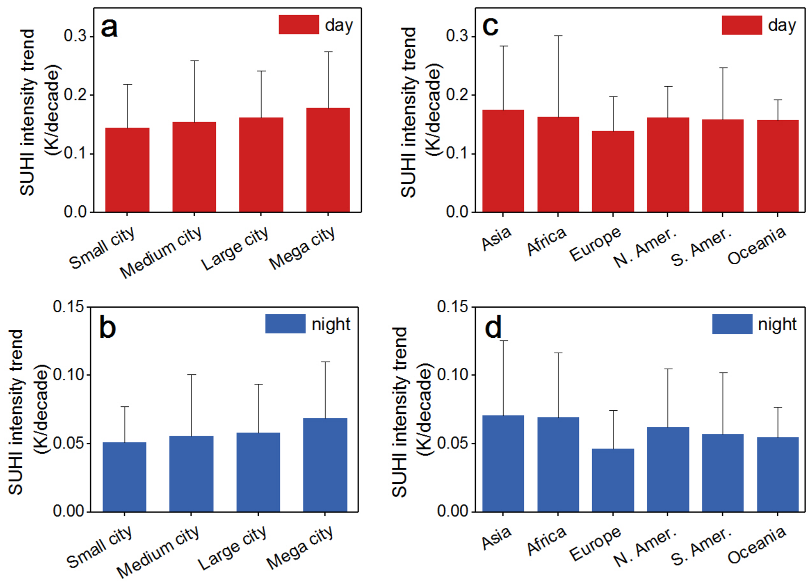

Supplementary Fig. 7 | Surface UHI intensity trends (quantified by the LST difference between the urban core and rural background) by city size and continent. Note that the error bars represent 10% ~ 90% percentiles.

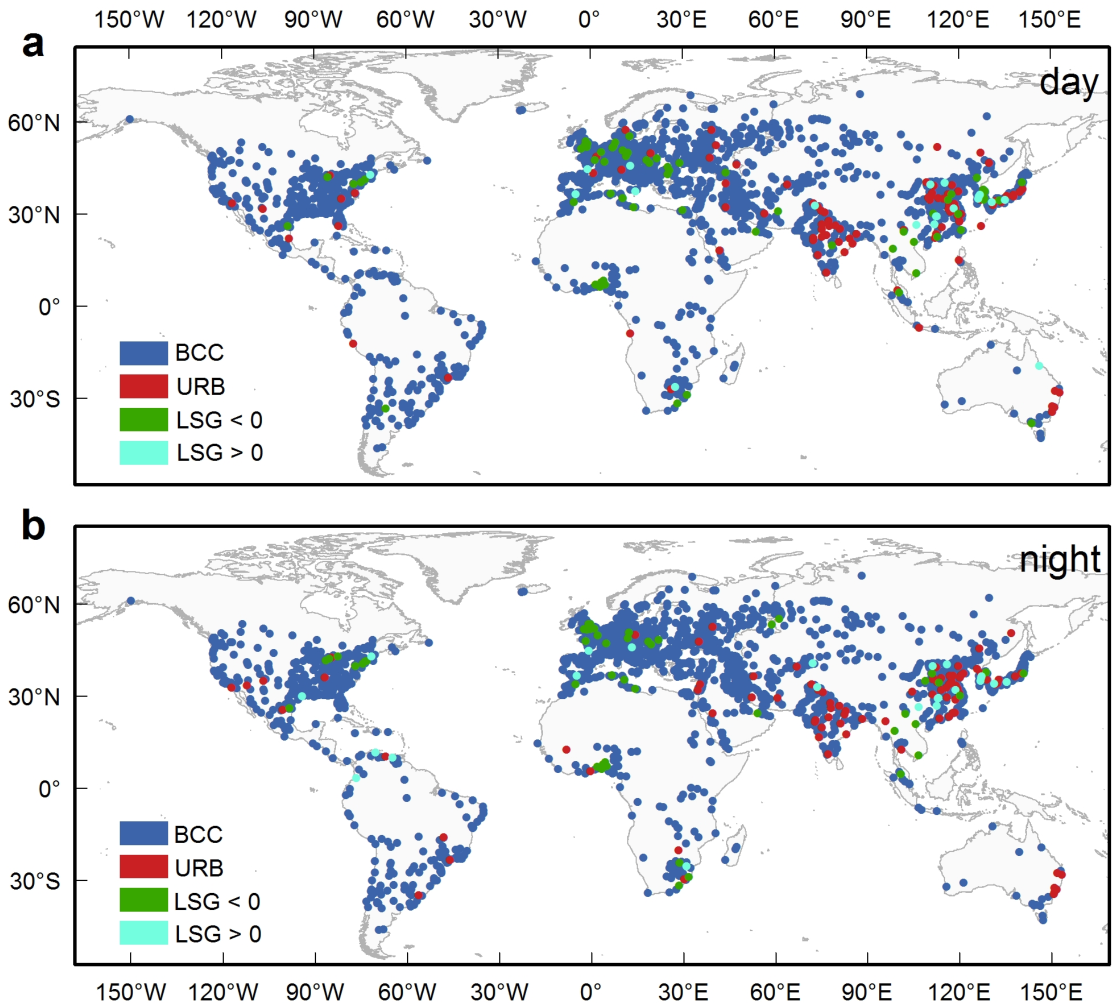

Supplementary Fig. 8 | Maps of the dominant contributor | Blue, red and green (dark and light) indicate that the dominant (or maximum) contributor to urban surface warming trend is background climate change (BCC), urbanization (URB) and landscape greening (LSG), respectively. Dark green and light green indicate that LGS contribution is negative and positive, respectively.

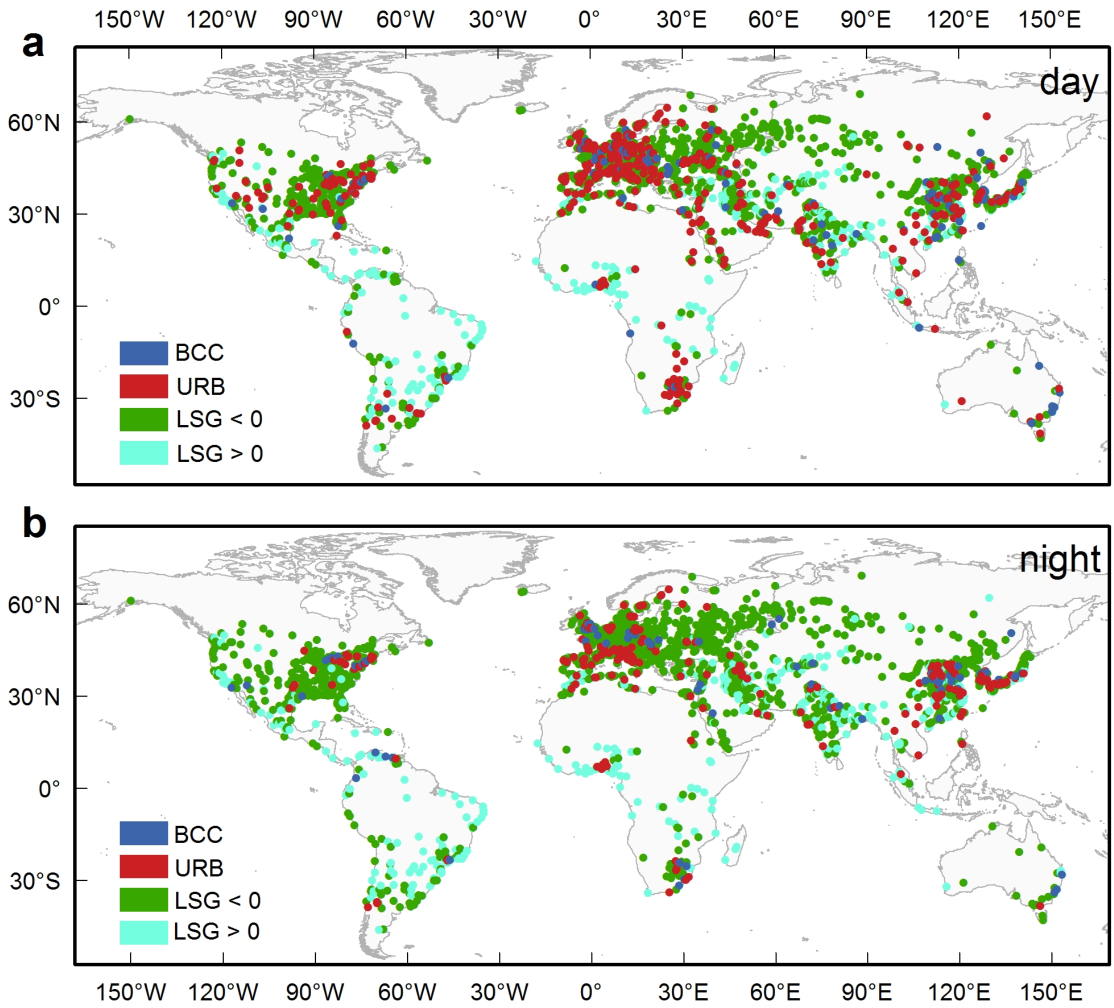

Supplementary Fig. 9 | Maps of the minimum contributor. Blue, red and green (dark and light) indicate that the minimum contributor to urban warming trend is background climate change (BCC), urbanization (URB) and landscape greening (LSG), respectively. Dark green and light green indicate that LGS contribution is negative and positive, respectively.

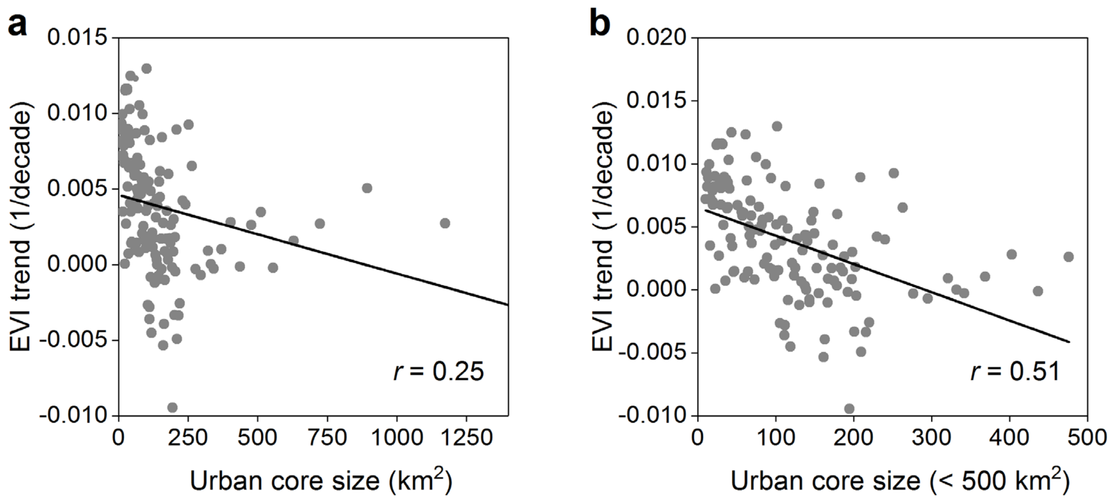

Supplementary Fig. 10 | Relationships between EVI trend and urban core size.

Relationships for global cities (**a**) and clusters with urban core size < 500 km^2 (**b**).

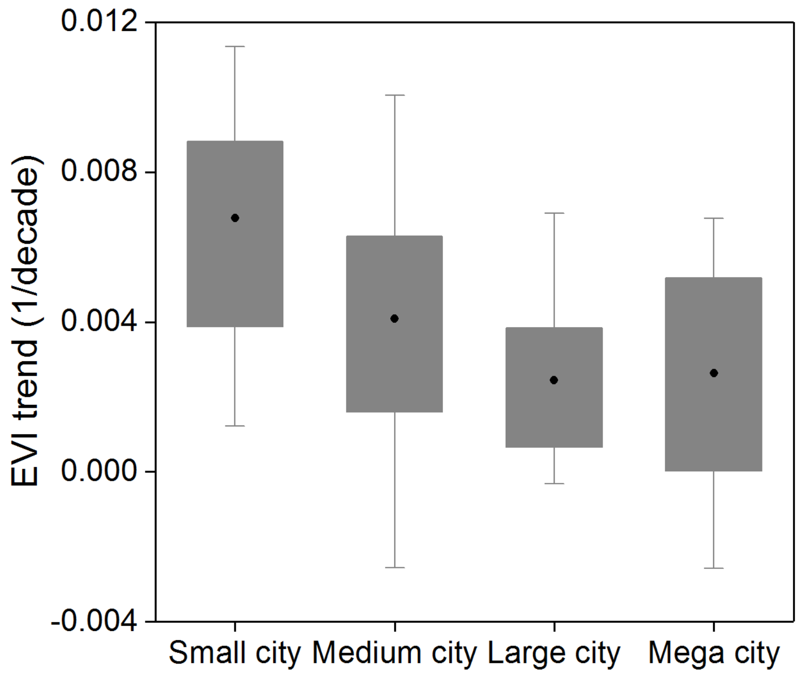

Supplementary Fig. 11 | EVI trends over urban core by city size. Note that the error bars represent 10% ~ 90% percentiles.

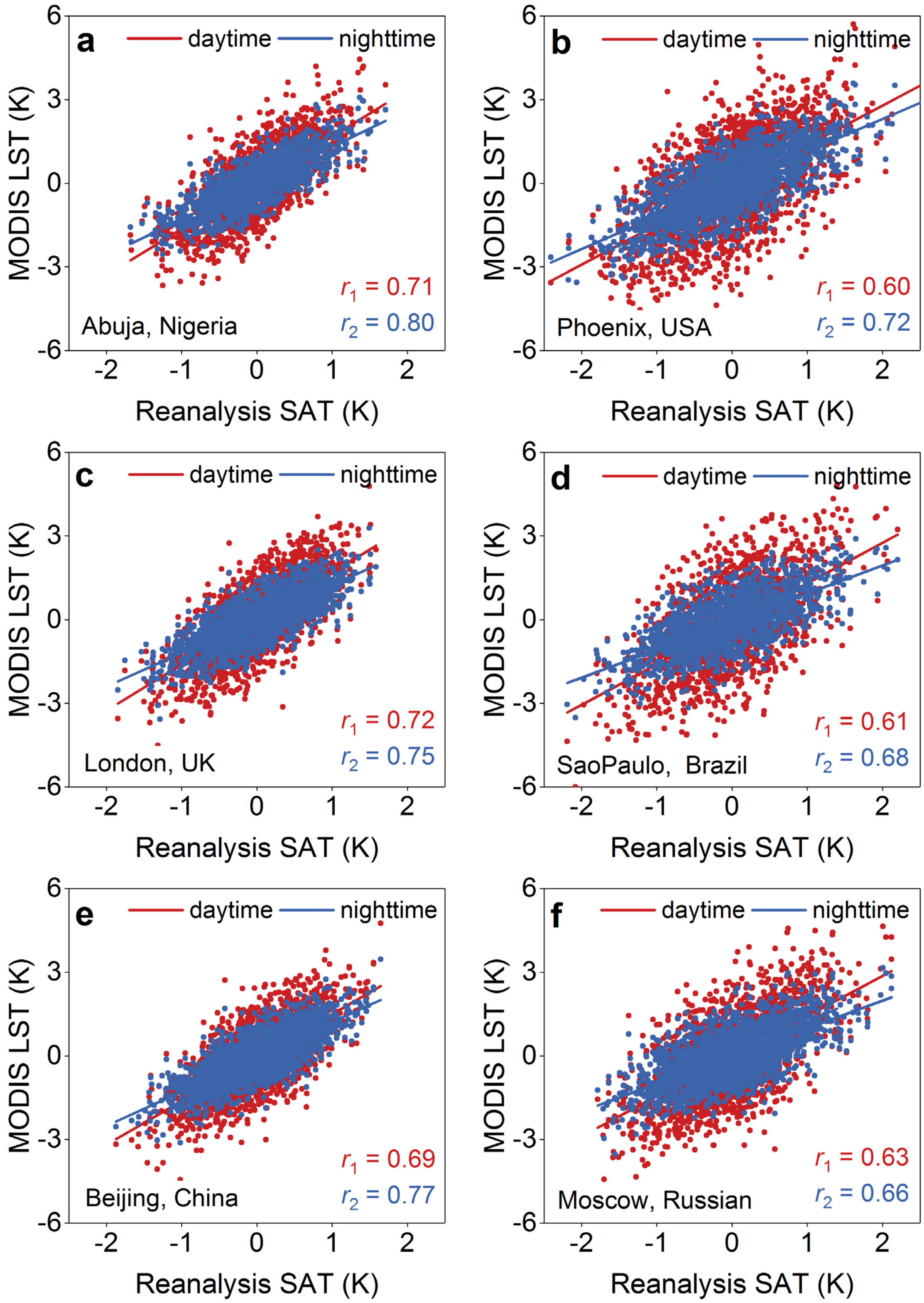

264

265 **Supplementary Fig. 12 | Relationships of temporal anomalies between MODIS**
266 **LST and reanalysis SAT over the rural background in six megacities |** They
267 include (**a**) Abujia (Nigeria), (**b**) Phoenix (USA), (**c**) London (UK), (**d**) SaoPaulo

(Brazil), (**e**) Beijing (China), and (**f**) Moscow (Russian). r_1 and r_2 are the Pearson's correlation coefficients between MODIS LST and reanalysis SAT for daytime and nighttime, respectively.

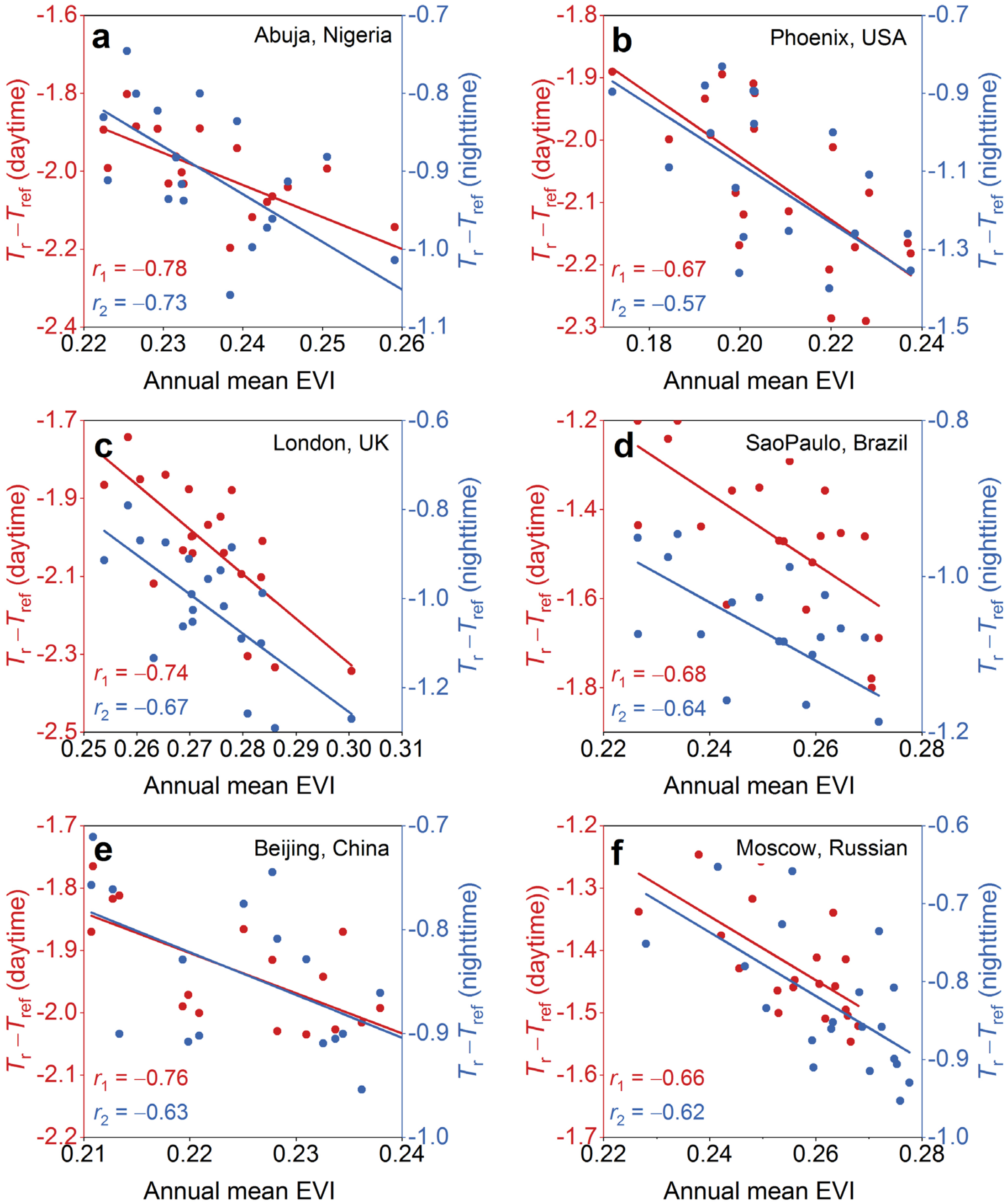

Supplementary Fig. 13 | Demonstration of the statistically negative relationships between the annual mean LST and EVI over the rural background in six megacities | They include (a) Abujia (Nigeria), (b) Phoenix (USA), (c) London (UK),

(d) SaoPaulo (Brazil), (e) Beijing (China), and (f) Moscow (Russian). r1 and r2 are the Pearson's correlation coefficients between MODIS LST and reanalysis SAT for daytime and nighttime, respectively.

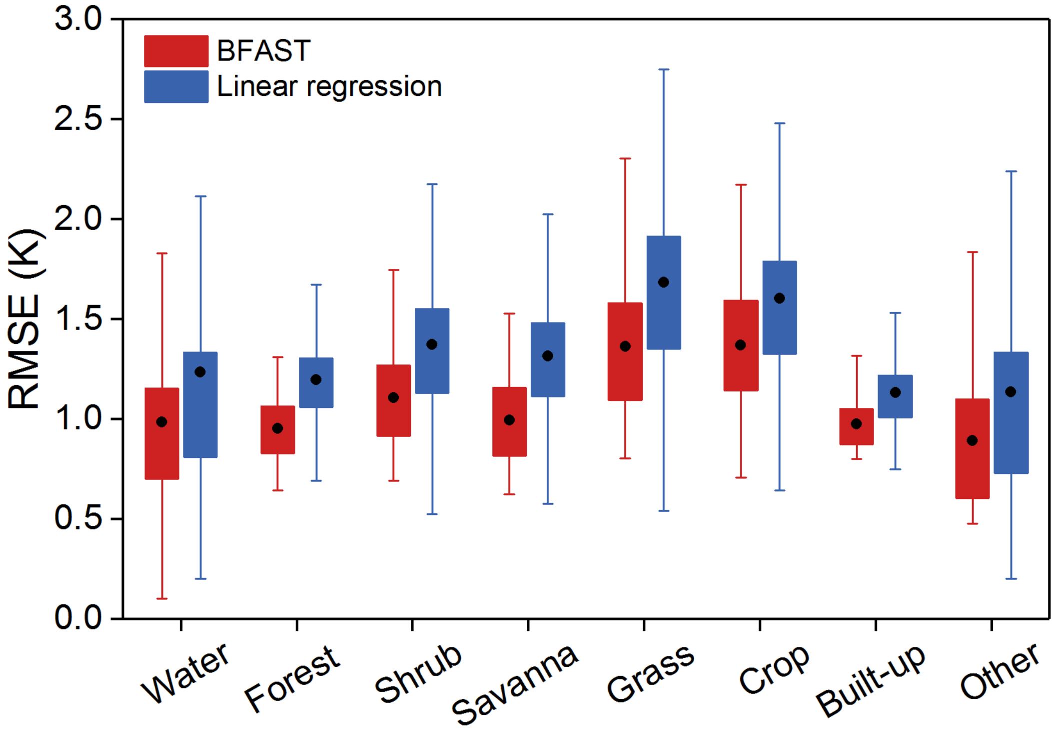

Supplementary Fig. 14 | Mean RMSEs (root mean square errors) of the BFAST algorithm and the linear regression over global cities for modelling daytime MODIS LSTs over different land cover types. Note that the error bars represent 10% ~ 90% percentiles.

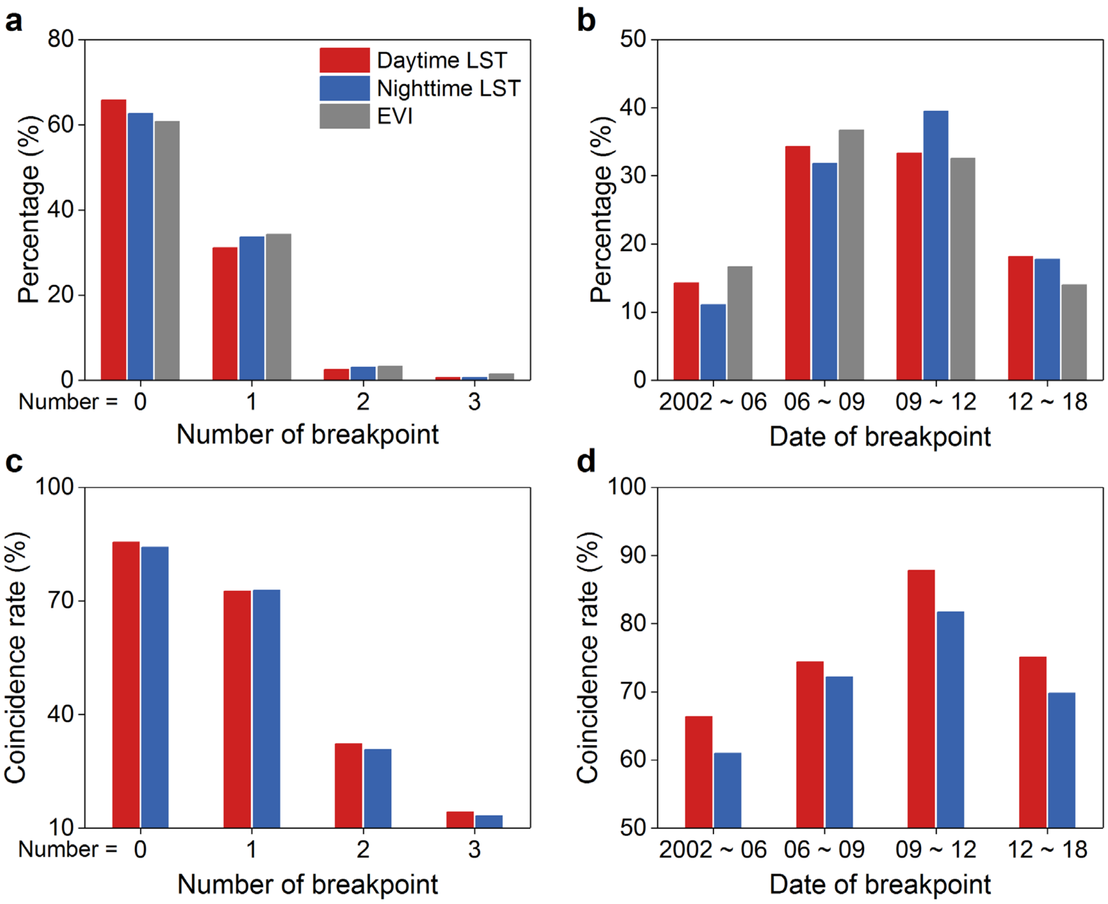

Supplementary Fig. 15 | Percentages of the number (a) and the date (b) for the breakpoints detected by the BFAST algorithm for the daytime (nighttime) LST and EVI, as well as the coincidence rates of the number (c) and date (d) of between the breakpoints detected from the daytime (nighttime) LST and EVI data.

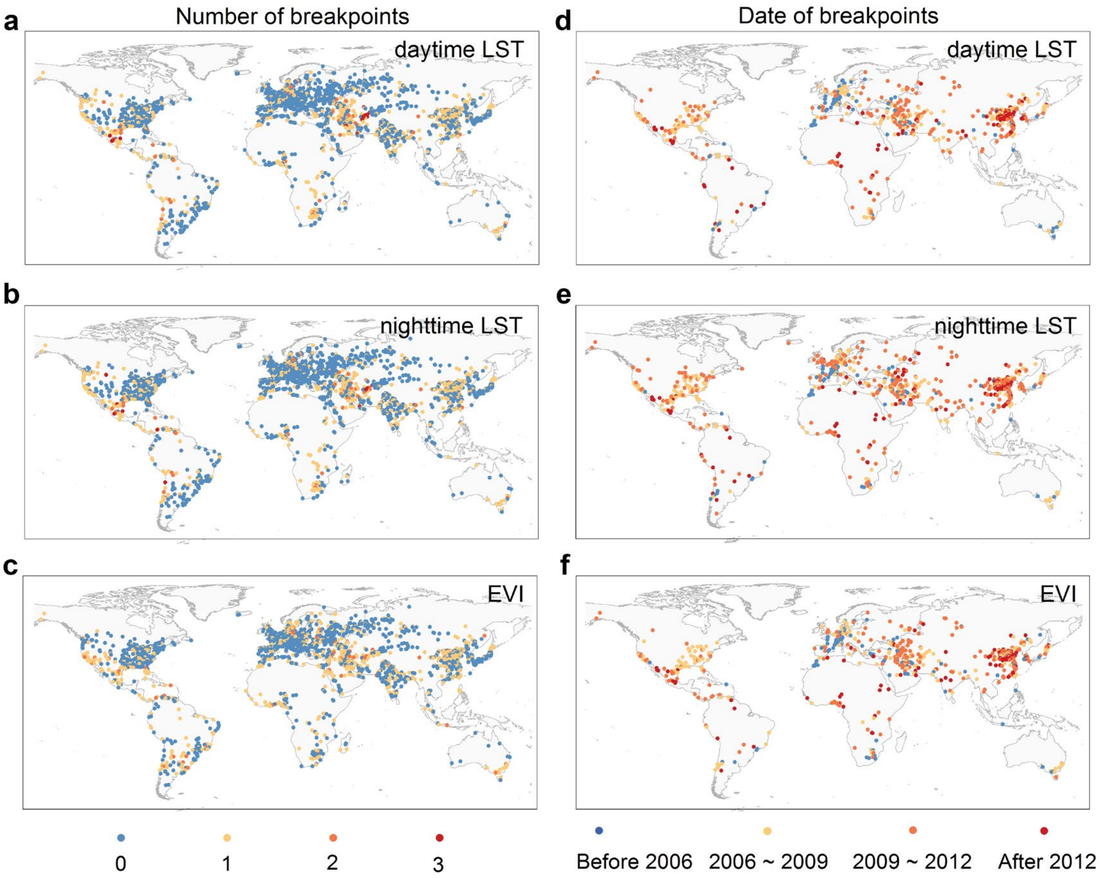

Supplementary Fig. 16 | Map of the breakpoint information identified by the BFAST algorithm | Number (the first column, **a**–**c**) and date (the second column, **d**–**f**) information of the breakpoints for daytime LST (**a** and **d**), nighttime LST (**b** and **e**), and EVI (**c** and **f**).

C. Supplementary Tables

Supplementary Table 1. The trends in LST/EVI over the urban core, rural background, and transitional surfaces.

LST/EVI	Surface type	Trends (annual)	Trends (summer)
daytime LST $K \cdot decade^{-1}$ (mean ± one S.D.)	urban core	0.60 ± 0.21	0.57 ± 0.26
	rural background	0.40 ± 0.23	0.42 ± 0.27
	transitional surface	1.06 ± 0.41	1.10 ± 0.43
nighttime LST $K \cdot decade^{-1}$ (mean ± one S.D.)	urban core	0.43 ± 0.16	0.44 ± 0.24
	rural background	0.37 ± 0.21	0.38 ± 0.22
	transitional surface	0.84 ± 0.39	0.85 ± 0.37
EVI $1 \cdot decade^{-1}$ (mean ± one S.D.)	urban core	0.0039 ± 0.0017	0.0044 ± 0.0025
	rural background	0.0083 ± 0.0026	0.0087 ± 0.0028
	transitional surface	−0.088 ± 0.025	−0.090 ± 0.027

Supplementary Table 2. The separate contributions from different drivers to urban warming for cities with different sizes. BCC, URB, and LSG represent background climate change, urbanization, and landscape greening, respectively.

	Control	Global	Small-cities	Medium-cities	Large-cities	Mega-cities
Daytime (mean ± one S.D)	**BCC**	0.34 ± 0.13	0.30 ± 0.092	0.32 ± 0.11	0.39 ± 0.17	0.37± 0.15
	URB	0.27 ± 0.13	0.20 ± 0.088	0.26 ± 0.13	0.31 ± 0.17	0.33± 0.16
	LSG	−0.10 ± 0.028	−0.14 ± 0.043	−0.13 ± 0.040	−0.072 ± 0.034	−0.079± 0.034
	Others	0.044 ± 0.023	0.049 ± 0.024	0.057 ± 0.028	0.035 ± 0.026	0.040± 0.029
Nighttime (mean ± one S.D)	**BCC**	0.25 ± 0.078	0.24 ± 0.073	0.24 ± 0.071	0.25± 0.080	0.25 ± 0.086
	URB	0.21 ± 0.094	0.18 ± 0.075	0.20 ± 0.084	0.24 ± 0.097	0.24 ± 0.12
	LSG	−0.052 ± 0.014	−0.087 ± 0.014	−0.055 ± 0.016	−0.040 ± 0.019	−0.037 ± 0.18
	Others	0.030 ± 0.013	0.041 ± 0.015	0.029 ± 0.015	0.024± 0.017	0.027 ± 0.017

Supplementary Table 3. Separate contributions from different drivers to urban warming for cities across continents.

	Control	Asia	Africa	Europe	North America	South America	Oceania
Daytime (mean ± one S.D)	**BCC**	0.41 ± 0.13	0.26 ± 0.066	0.32 ± 0.10	0.36 ± 0.14	0.26 ± 0.15	0.37 ± 0.13
	URB	0.38 ± 0.17	0.25 ± 0.082	0.24 ± 0.084	0.25 ± 0.11	0.16 ± 0.043	0.25 ± 0.12
	LSG	−0.14 ± 0.039	0.053 ± 0.024	−0.17 ± 0.044	−0.085± 0.050	0.049 ± 0.022	−0.12 ± 0.057
	Others	0.056 ± 0.013	0.034 ± 0.014	0.043 ± 0.012	0.038 ± 0.020	0.037 ± 0.019	0.030 ± 0.011
Nighttime (mean ± one S.D)	**BCC**	0.29 ± 0.054	0.21 ± 0.057	0.26 ± 0.12	0.25 ± 0.12	0.20 ± 0.096	0.24 ± 0.073
	URB	0.28 ± 0.082	0.21 ± 0.059	0.22 ± 0.11	0.18 ± 0.091	0.14 ± 0.034	0.16 ± 0.073
	LSG	−0.070± 0.021	0.041 ± 0.016	−0.10 ± 0.025	−0.043 ± 0.022	0.022 ± 0.0098	−0.059 ± 0.019
	Others	0.033 ± 0.015	0.024 ± 0.014	0.032 ± 0.016	0.029 ± 0.0068	0.031 ± 0.012	0.033 ± 0.013

Supplementary Table 4. The ratios between LST and population density (or EVI) trends over urban areas among continents.

	LST_{POP} (K decade^{-1})	**POD (km^2)**	**$\text{Ratio}_{\_POD}$ (×10^2)**	**LST_{EVI} (K decade^{-1})**	**EVI (decade^{-1})**	**$\text{Ratio}_{_EVI}$ (×10^{-2})**
Global	0.34	353	0.10	0.10	0.0039	0.26
Asia	0.41	716	0.06	0.14	0.0024	0.58

Africa	0.26	1052	0.03	−0.05	−0.0088	0.06
Europe	0.32	151	0.21	0.17	0.012	0.14
North America	0.36	123	0.29	0.09	0.0017	0.50
South America	0.26	397	0.07	−0.05	−0.0091	0.05
Oceania	0.37	58	0.64	0.12	0.0052	0.23

Note: LST_{POD} and LST_{EVI} (K decade^{-1}) represent the variations of urban LST trends induced by population density and EVI (K decade^{-1}) trends, respectively; POD denotes the population density; $Ratio\_{POD}$ (or $Ratio\_{EVI}$) is the ratio between LST_{POD} and POD (or EVI).

Supplementary Table 5. List of major acronyms and abbreviations used in this study

Abbreviations	Description
LST	Land surface temperature
SAT	Near-surface air temperature
EVI	Enhanced vegetation index
UHI	Urban heat island
SUHI	Surface urban heat island
BFAST	Breaks For Additive Season and Trend
URB	Background climate change
BCC	Urbanization
LSG	Landscape greening
T_{OBS}	The observed increment of annual mean urban LST as referenced to the annual mean value at the previous year
T_{BCC}	Temperature increment signals attributed to BCC
T_{URB}	Temperature increment signals attributed to URB
T_{LSG}	Temperature increment signals attributed to LSG
β_{BCC}	Scaling factor of T_{BCC}
β_{URB}	Scaling factor of T_{URB}
β_{LSG}	Scaling factor of T_{LSG}
v_{BCC}	Noise from internal variability in T_{BCC}
v_{URB}	Noise from internal variability in T_{URB}
v_{LSG}	Noise from internal variability in T_{LSG}
ε	Residual error term

D. Supplementary References

1. Mildrexler, D. J., Zhao, M. & Running, S. W. A global comparison between station air temperatures and MODIS land surface temperatures reveals the cooling role of forests. *J. Geophys. Res. Biogeosci.* **116**, G03025 (2011).
2. Dyce, D. R. & Voogt, J. A. The influence of tree crowns on urban thermal effective anisotropy. *Urban Clim.* **23**, 91–113 (2018).
3. Hu, L., Monaghan, A. J., Voogt, J. A. & Barlage, M. A first satellite-based observational assessment of urban thermal anisotropy. *Remote Sens. Environ.* **181**, 111–121 (2016).
4. Oke, T. R., Mills, G., Christen, A. & Voogt, J. A. Urban climate. Cambridge University Press. (2017).
5. Venter, Z. S., Chakraborty, T. & Lee, X. Crowdsourced air temperatures contrast satellite measures of the urban heat island and its mechanisms. *Sci. Adv.* **7**, eabb9569 (2021).
6. Wang, K. et al. Comparing the diurnal and seasonal variabilities of atmospheric and surface urban heat islands based on the Beijing urban meteorological network. *J. Geophys. Res. Atmos.* **122**, 2131–2154 (2017).
7. Li, X. et al. Global urban growth between 1870 and 2100 from integrated high resolution mapped data and urban dynamic modeling. *Commun. Earth Environ.* **2**, 1–10 (2021).
8. Mann, H. B. & Whitney, D. R. On a test of whether one of two random variables is stochastically larger than the other. *The annals of mathematical statistics*, 50–60 (1947).
9. Pugachev, V. S. Probability theory and mathematical statistics for engineers. Elsevier (2014).
10. Rice, J. A. Mathematical statistics and data analysis. Cengage Learning (2006).
11. Chakraborty, T. & Lee, X. A simplified urban-extent algorithm to characterize surface urban heat islands on a global scale and examine vegetation control on

their spatiotemporal variability. *Int. J. Appl. Earth Obs. Geoinf.* **74**, 269–280 (2019).

12. Yao, R. et al. Greening in rural areas increases the surface urban heat island intensity. *Geophys. Res. Lett.* **46**, 2204–2212 (2019).
13. Liu, Z. et al. Taxonomy of seasonal and diurnal clear-sky climatology of surface urban heat island dynamics across global cities. *ISPRS J. Photogramm. Remote Sens.* **187**, 14–33 (2022).
14. Zhou, D. et al. Climate–vegetation control on the diurnal and seasonal variations of surface urban heat islands in China. *Environ. Res. Lett.* **11**, 074009 (2016).
15. Zhou, D. et al. Surface urban heat island in China's 32 major cities: Spatial patterns and drivers. *Remote Sens. Environ.* **152**, 51–61 (2014).
16. Lai, J. et al. Meteorological controls on daily variations of nighttime surface urban heat islands. *Remote Sens. Environ.* **253**, 112198 (2021).
17. Manoli, G. et al. Magnitude of urban heat islands largely explained by climate and population. *Nature* **573**, 55–60 (2019).
18. She, Y. et al. Strong regulation of daily variations in nighttime surface urban heat islands by meteorological variables across global cities. *Environ. Res. Lett.*, 014049 (2021).
19. Estrada, F. & Perron, P. Disentangling the trend in the warming of urban areas into global and local factors. *Ann. N. Y. Acad. Sci* **1504**, 230–246 (2021).
20. Estrada, F., Kim, D. & Perron, P. Anthropogenic influence in observed regional warming trends and the implied social time of emergence. *Commun. Earth Environ.* **2**, 1–9 (2021).
21. Swanson, K. L., Sugihara, G. & Tsonis, A. A. Long-term natural variability and 20th century climate change. *Proc. Natl. Acad. Sci. USA* **106**, 16120–16123 (2009).
22. Wu, Z. et al. On the time-varying trend in global-mean surface temperature. *Clim. Dynam.* **37**, 759–773 (2011).

23. NourEldeen, N. et al. Analysis of the spatiotemporal change in land surface temperature for a long-term sequence in Africa (2003–2017). *Remote Sens.* **12**, 488 (2020).
24. Tayyebi, A., Shafizadeh-Moghadam, H. & Tayyebi, A. H. Analyzing long-term spatio-temporal patterns of land surface temperature in response to rapid urbanization in the mega-city of Tehran. *Land Use Policy* **71**, 459–469 (2018).
25. Tomlinson, C. J., Chapman, L., Thornes, J. E. & Baker, C. Remote sensing land surface temperature for meteorology and climatology: a review. *Meteorol. Appl.* **18**, 296–306 (2011).
26. Zhou, D. et al. Croplands intensify regional and global warming according to satellite observations. *Remote Sens. Environ.*, 112585 (2021).
27. Verbesselt, J., Hyndman, R. J., Newnham, G. & Culvenor, D. S. Detecting trend and seasonal changes in satellite image time series. *Remote Sens. Environ.* **114**, 106–115 (2010).
28. Bechtel, B. Robustness of annual cycle parameters to characterize the urban thermal landscapes. *IEEE Geosci. Remote Sens. Lett.* **9**, 876–880 (2012).
29. Quan, J. et al. Time series decomposition of remotely sensed land surface temperature and investigation of trends and seasonal variations in surface urban heat islands. *J. Geophys. Res. Atmos.* **121**, 2638–2657 (2016).
30. Huang, K. et al. Projecting global urban land expansion and heat island intensification through 2050. *Environ. Res. Lett.* **14**, 114037 (2019).
31. Liu, X. et al. High-spatiotemporal-resolution mapping of global urban change from 1985 to 2015. *Nat. Sustain.* **3**, 564–570 (2020).